

## Research Paper

# Precipitate evolution in laser metal deposited Haynes 282 investigated using a combination of synchrotron scattering experiment and multi-scale modeling

Martin Fisk<sup>a,b</sup>, Anders Ericsson<sup>b</sup>, Manon Bonvalet Rolland<sup>c</sup>, Erik Granhed<sup>c</sup>,  
 Johan Hektor<sup>a</sup>, Alexander Dahlström<sup>c</sup>, Jesper Silwer<sup>d</sup>, Ceena Joseph<sup>d</sup>, Petter Persson<sup>e</sup>,  
 Greta Lindwall<sup>c</sup>

<sup>a</sup> Materials Science and Applied Mathematics, Malmö University, SE 205 06 Malmö, Sweden

<sup>b</sup> Division of Solid Mechanics, Lund University, P.O. Box 118, SE 221 00 Lund, Sweden

<sup>c</sup> Department of Materials Science and Engineering, Royal Institute of Technology (KTH), SE 114 28, Stockholm, Sweden

<sup>d</sup> GKN Aerospace Sweden AB, Flygmotorvägen 1, SE 461 81 Trollhättan, Sweden

<sup>e</sup> Alleima, SE 811 81 Sandviken, Sweden

## ARTICLE INFO

## Keywords:

Small- and wide-angle X-ray scattering (SAXS/WAXS)  
 Atom probe tomography (APT)  
 Superalloy  
 Additive manufacturing

## ABSTRACT

The Ni-based superalloy Haynes 282 exhibits rapid  $\gamma'$  precipitation kinetics, and experimental studies have shown the formation of in-process precipitates in samples produced using the direct energy deposition additive manufacturing method, laser metal deposition (LMD). Understanding how these precipitates form and influence the final microstructure is essential for predicting and controlling the mechanical properties of processed Haynes 282. In this study, the particle size and volume fraction of  $\gamma'$  precipitates formed in LMD samples are simulated using classical nucleation and growth theory (CNGT). To account for the thermal history during manufacturing, the precipitate model is implemented as a multi-scale framework integrated into a finite element software. Calphad thermodynamic and diffusion data descriptions are used as input to the CNGT model to simulate the precipitation kinetics during different heat treatments. The simulated results are compared with experimental data obtained from small- and wide-angle X-ray scattering, as well as from atom probe tomography. The simulations show good agreement with experimental findings, demonstrating that thermodynamic databases can be used to accurately simulate precipitate evolution in LMD-processed Haynes 282 using CNGT.

## 1. Introduction

Laser metal deposition (LMD) is a directed energy deposition additive manufacturing (AM) technique that operates by feeding metal powder or wire through a nozzle into a melt pool created by a focused laser beam [1]. It is a suitable choice for applications such as repair welding [2], as well as for the fabrication of functionally graded metallic materials, which integrate two or more materials to achieve a gradual transition in properties such as strength, hardness, or thermal resistance across a component [3]. The feedstock materials in LMD are not limited to pure metals, and LMD has, for example, been successfully employed to produce functional metal matrix composites based on the superalloy Haynes 282, reinforced with various grades of SiC particles [4].

Haynes 282 is a relatively new Ni-based superalloy that is primarily strengthened by the formation of intra-granular secondary  $\gamma'$  precipitates composed of Ni, Al, and Ti. The  $\gamma'$  phase is commonly represented stoichiometrically as Ni<sub>3</sub>(Al,Ti). This alloy exhibits excellent creep resistance and thermal stability at elevated temperatures, making it well suited for high-temperature structural applications [5,6]. To better understand the mechanisms governing the growth and coarsening of the  $\gamma'$  phase, Mukherjee et al. [7] identified the rate-controlling elements using atom probe tomography (APT), transmission electron microscopy (TEM), and X-ray diffraction (XRD), combined with simulations of the precipitation kinetics using the Thermo-Calc Software package TC-Prisma [8]. They concluded that growth kinetics are primarily controlled by the diffusion of Cr away from, and Ti toward, the

\* Corresponding author at: Materials Science and Applied Mathematics, Malmö University, SE 205 06 Malmö, Sweden.

E-mail addresses: [martin.fisk@mau.se](mailto:martin.fisk@mau.se) (M. Fisk), [anders.ericsson1@saabgroup.com](mailto:anders.ericsson1@saabgroup.com) (A. Ericsson), [manon.rolland@univ-lille.fr](mailto:manon.rolland@univ-lille.fr) (M.B. Rolland), [erik.granhed@geaerospace.com](mailto:erik.granhed@geaerospace.com) (E. Granhed), [Johan.Hektor@mau.se](mailto:Johan.Hektor@mau.se) (J. Hektor), [alexander.dahlstroem@vattenfall.com](mailto:alexander.dahlstroem@vattenfall.com) (A. Dahlström), [jesper.silwer@gknaerospace.com](mailto:jesper.silwer@gknaerospace.com) (J. Silwer), [joseph.ceena@gknaerospace.com](mailto:joseph.ceena@gknaerospace.com) (C. Joseph), [petter.a.persson@alleima.com](mailto:petter.a.persson@alleima.com) (P. Persson), [gretal@kth.se](mailto:gretal@kth.se) (G. Lindwall).

<https://doi.org/10.1016/j.addma.2026.105093>

Received 8 October 2025; Received in revised form 19 December 2025; Accepted 21 January 2026

Available online 3 February 2026

2214-8604/© 2026 The Authors. Published by Elsevier B.V. This is an open access article under the CC BY license (<http://creativecommons.org/licenses/by/4.0/>).

**Table 1**

Provided composition (in weight percent) of the powder used for the LMD manufacturing process.

Ni	Cr	Co	Mo	Ti	Al	Fe	C
Balance	19.5	10.2	8.30	2.16	1.61	0.2	0.05

$\gamma'$  phase. For longer ageing times (greater than four days at 760 °C), when coarsening becomes the dominant mechanism, the rate is mainly governed by the diffusion of Mo through the matrix, away from the precipitate interface. Similarly, Ramakrishnan and Dinda [4] investigated the precipitation kinetics of both the  $\gamma'$  phase and carbide phase experimentally supported by Calphad thermodynamic calculations. They also examined the microstructure and mechanical properties of as-deposited and heat-treated LMD Haynes 282 samples using scanning electron microscopy (SEM), energy-dispersive X-ray spectroscopy (EDS), XRD, uniaxial tensile testing, and microhardness measurements.

One property of the Haynes 282 alloy is its rapid nucleation behavior. Even after quenching from temperatures that fully dissolve the  $\gamma'$  phase, a detectable volume fraction of precipitates has been reported [9,10]. The  $\gamma'$  phase has also been observed in as-built LMD components [7]. Although precipitate formation has been experimentally detected during the building process, further insight could be gained by simulating the precipitation kinetics during manufacturing in order to better understand the nucleation behavior. An additional open question is whether precipitates formed during LMD influence the final precipitate distribution after a subsequent post-build ageing heat treatment of the alloy.

In this study, the formation of  $\gamma'$  precipitates in an LMD-manufactured Haynes 282 component is simulated using the classical nucleation and growth theory (CNGT), implemented as a multi-scale framework within a finite element (FE) software. Calphad thermodynamic and diffusion data are used as input, allowing for general application across a wide range of temperatures, and compositions. The simulation results are compared with experimental data obtained from high-energy synchrotron small- and wide-angle X-ray scattering (SAXS/WAXS) as well as APT. To investigate the influence of in-process nucleated precipitates on the final microstructure, both as-built and solution heat-treated samples are subjected to ageing heat treatments and analyzed using SAXS. These results are further compared with simulations assuming no initial precipitates, and an alternative heat treatment route – consisting of full dissolution followed by controlled cooling – is also evaluated to study its effect on precipitate evolution.

## 2. Sample preparation and experiments

Three samples of Haynes 282 were manufactured on alloy 718 build plates using the powder LMD technique. The powder had a specified particle-size range of 45–75  $\mu\text{m}$ , and its chemical composition is given in Table 1. Each sample was produced by depositing ten layers with six beads per layer. A laser power of 3 kW, a spot size of 4 mm, and a scanning speed of 33 mm  $\text{s}^{-1}$  were used for all builds. The layer height varied between 1.0 mm and 1.2 mm, while the build width was approximately 11 mm. The cooling time between beads was approximately 7 s, and between layers about 55 s. During the build process, the scanning direction was reversed from one layer to the next. The experimental setup is shown in Fig. 1.

To measure the temperature during the process, two type-K thermocouples were mounted on the backside of the build plate. An illustration of the fixture configuration, sample geometry, and thermocouple locations is shown in Fig. 2. In addition, a third thermocouple was attached to the fixture clamps. The recorded temperatures for build plate no. 1 are presented in Fig. 3. The blue curve corresponds to the thermocouple located at the center of the test plate (TC-Center in Fig. 2), while the red curve corresponds to the thermocouple positioned near the edges

of the build plate (TC-Outer in Fig. 2). The temperature measured at the fixture clamps is shown in black. A temporary interruption in the data acquisition resulted in a short period of missing values. Nevertheless, this particular sample was used in the synchrotron experiments described in Section 2.1, and the corresponding temperature data are therefore presented here.

After the building process, samples no. 2 and no. 3 underwent ageing heat treatment. Sample no. 2 was directly aged at 788 °C for 8 h. Sample no. 3, on the other hand, was first solution heat-treated at 1120 °C for 2 h, then heat-treated at 1010 °C for 2 h, and finally aged at 788 °C for 8 h. The particle size and corresponding phases were measured using SAXS and WAXS, as described in Section 2.1.

### 2.1. Synchrotron experiments

Combined high-energy SAXS and WAXS measurements were conducted at the Swedish Material Science Beamline (P21.2), DESY, Germany using a beam energy of 68.5 keV and a beam size of 0.5  $\times$  0.5 mm. The WAXS pattern was detected using four VAREX XRD4343CT detectors positioned 1.35 m behind the sample, with an exposure time of 0.1 s. The sample-to-detector distance was calibrated using a LaB<sub>6</sub> standard. The SAXS pattern was recorded using an EIGER X 4M detector positioned 14 m behind the sample, with an exposure time of 3 s. A vacuum flight tube was placed between the sample and the SAXS detector to minimize noise. The sample-to-detector distance for the SAXS measurement was calibrated using an AgBh standard.

### 2.2. Atom probe tomography

Atom probe tomography (APT) was carried out using an EIKOS-UV (TM) instrument from CAMECA Instrument Inc., equipped with a 355 nm laser. Samples were prepared using a FEI Nova 600 NanoLab dual beam system using the classic lift-out method onto tungsten needle geometry pre-tips [11]. Final cleaning of the tips was made using 5 kV, 29 pA with a scan speed of 10  $\mu\text{s}$ .

The APT measurements were carried out at 40 K, with a pulse rate of 200 kHz, using constant flux mode, and auto-pulse energy control. The constant areal evaporation was 81.65 % $\mu\text{m}^{-2}$  (resulting in a detection rate of 0.2 %–0.79 %). The charge state ratio Ni<sup>+</sup>/Ni<sup>++</sup> = 5 was used for pulse energy control in accordance with Tegg et al. [12]. Data was collected at 5.9–11 Torr, with a background of 14 ppm ns<sup>-1</sup> in the voltage range 5.2–9.0 kV.

The 3D reconstruction of the tips was performed using APSuite 6.1 in dynamic voltage reconstruction mode [13], with an image compression factor of 1.3, a field factor of 3.72, and an initial radius of 50 nm. The choice of image compression and field factor depends on the electrostatic environment determined by the instrument design. Prior to the measurements, the system was calibrated using a spatial distribution map obtained from a pure Al sample, following the procedure described in [14]. The initial tip radius was corrected based on SEM imaging after final FIB cleaning of the tip.

## 3. Finite element model

The LMD building process is modeled using the FE method. The program numerically solves the heat transport equation [15]

$$\rho c_p \frac{\partial T}{\partial t} - \nabla \cdot (\kappa \nabla T) = Q \quad (1)$$

where  $\rho$  is the density of the material,  $c_p(T)$  is the temperature-dependent specific heat capacity, and  $\kappa(T)$  is the temperature-dependent thermal conductivity matrix. Isotropic conductivity is assumed. The temperature-dependent material properties for Haynes 282 and alloy 718 were provided by JMatPro [16]. The latent heat due to phase changes is taken into account using the enthalpy method, where an effective heat capacity is computed and used over a time step [17]. This method ensures that the latent heat is included even for larger

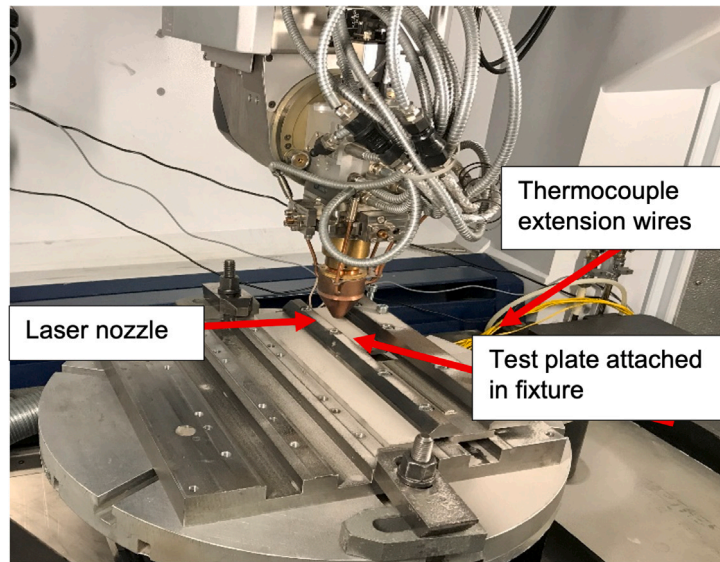


Fig. 1. Experimental LDM setup. The build is made in Haynes 282 and the build plate is made of alloy 718.

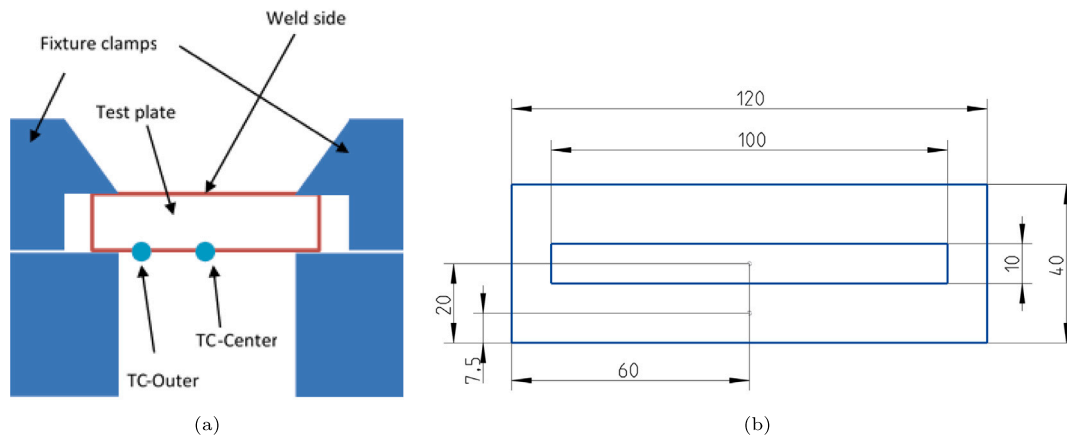


Fig. 2. Dimensions of test plate and position of thermocouples. (a) Illustrate how the build plate was fixated during the LMD process and (b) show the dimensions of the LMD build, build plate and the positions of the thermocouples. The build plate was 9.5 mm thick.

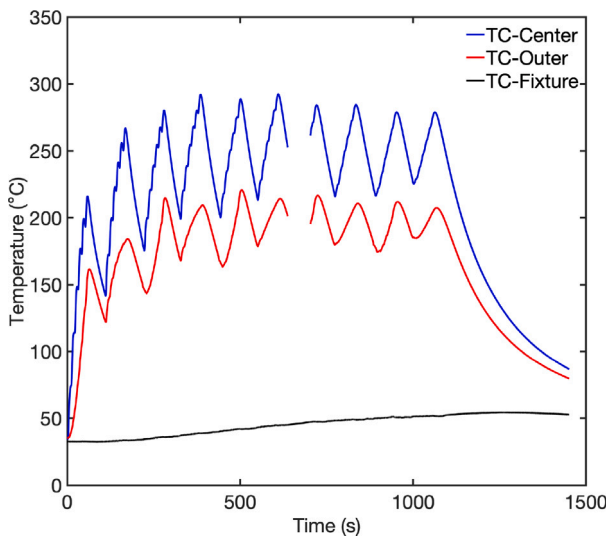


Fig. 3. Measured temperatures at the thermocouples for sample no. 1. An interruption in the temperature recording resulted in some data losses.

temperature changes within a time step. Values between extracted data points are linearly interpolated.

The heat arising from the laser-material interaction during the welding process is modeled as a volumetric heat source  $Q$  using the Goldak model [18]. In the model, the spatial distribution of the moving heat source is described using two Gaussian distributions, one for the heat distribution in the front  $Q_f$  and one for the heat distribution in the rear  $Q_r$ . The heat input is then defined in a local coordinate system moving with the heat source so that [17,19],

$$Q = \begin{cases} Q_f x' \geq 0 \\ Q_r x' < 0 \end{cases} \quad (2)$$

where respective heat distribution is formulated to be

$$Q_f = f_f \frac{12\sqrt{3}\eta P}{a_f b c \pi \sqrt{\pi}} \exp\left(-\frac{3x'^2}{a_f^2}\right) \exp\left(-\frac{3y'^2}{b^2}\right) \exp\left(-\frac{3z'^2}{c^2}\right) \quad (3a)$$

$$Q_r = (1 - f_f) \frac{12\sqrt{3}\eta P}{a_r b c \pi \sqrt{\pi}} \exp\left(-\frac{3x'^2}{a_r^2}\right) \exp\left(-\frac{3y'^2}{b^2}\right) \exp\left(-\frac{3z'^2}{c^2}\right) \quad (3b)$$

and  $x'$ ,  $y'$  and  $z'$  represent local coordinates with origin in the center, longitudinal, transverse, and downward directions of the heat source, respectively. The parameter  $f_f$  distributes heat between forward and rear parts.  $\eta$  is the laser efficient coefficient and is calibrated against

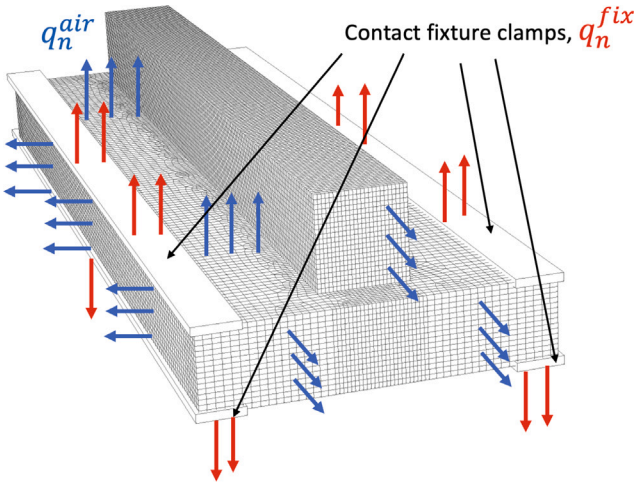


Fig. 4. The mesh of the FE model consisting of 242 224 hexahedral elements. The boundary conditions are illustrated.

the thermal measurements, see Section 5.1, and  $P$  is the laser power. The parameters  $a_f$ ,  $a_r$ ,  $b$  and  $c$  are characteristic lengths that defines the spatial distribution of the heat source. To make the heat source function continuous, the following relation between the power in the forward and rear parts need to be fulfilled

$$\frac{f_f}{a_f} = \frac{1 - f_f}{a_r} \quad (4)$$

The modeling domain is shown in Fig. 4. The mesh consists of 242 224 first-order hexahedral elements. The specific heat capacity and thermal conductivity of alloy 718 are assigned to the elements representing the base plate, while the elements in the LMD build are assigned the thermophysical properties of Haynes 282. The elements in the LMD build are initially deactivated and are successively activated as the heat source traverses the material and the temperature decreases.

A build comprising ten layers is simulated, represented by 20 elements in height and 24 elements in width. The total size of the LMD build is 100 mm in length, 10 mm in width, and 11 mm in height, deposited on a base plate measuring 120 mm in length, 40 mm in width, and 9.5 mm in thickness.

The boundary conditions used in the FE model are illustrated in Fig. 4. Between the test plate and the fixture clamps, small gaps invariably filled with air exist as a result of surface roughness, which introduces convection resistance [20]. The heat flux in the contact fixture clamps are therefore modeled as [21]

$$q_n^{\text{fix}} = h_{\text{fix}} (T - T_{\text{fix}}(t)), \quad (5)$$

where  $h_{\text{fix}}$  is an effective thermal conductance representing the contact, and  $T_{\text{fix}}$  is the temperature of the fixture clamps. As shown in Fig. 3, the temperature of the fixture clamps increases with time as heat is conducted from the base plate and accumulates in the clamps. To account for this,  $T_{\text{fix}}$  is allowed to vary as a function of time, and the measured values presented in Fig. 3 are used in Eq. (5). The thermal conductance  $h_{\text{fix}}$  is calibrated against the thermal measurements, as described in Section 5.1.

At the remaining boundaries, where the baseplate is surrounded by air, convective heat flow and radiation is applied. The heat flux at these boundaries  $q_n^{\text{air}}$  is expressed as

$$q_n^{\text{air}} = h_{\text{air}} (T - T_{\infty}) + \sigma_B \epsilon (T^4 - T_{\infty}^4) \quad (6)$$

where  $h_{\text{air}}$  is the coefficient of heat transfer to the air,  $T_{\infty}$  is the ambient temperature,  $\sigma_B$  is the Stefan–Boltzmann constant and  $\epsilon$  is the emissivity of the material.

#### 4. Precipitation model

The thermal FE model is coupled to a precipitation model that predicts the precipitate size distribution as a function of time and temperature. The model description is based on the CNGT valid for multicomponent alloys with small supersaturations in the matrix developed by Philippe and Vorhees [22,23].

According to classical nucleation theory, the nucleation rate is expressed as [24,25]

$$I = N_0 Z \beta^* \exp\left(-\frac{\Delta G^*}{k_B T}\right) \exp\left(\frac{\tau}{t}\right) \quad (7)$$

where  $N_0$  is the number of nucleation sites per unit volume,  $Z$  is the Zeldovich factor,  $\beta^*$  is the atomic attachment rate at the nucleus interface,  $k_B$  is the Boltzmann constant,  $T$  is the absolute temperature,  $t$  is the time,  $\tau = (4\pi\beta^* Z^2)^{-1}$  is the incubation time, and  $\Delta G^*$  is the nucleation barrier. It is given by

$$\Delta G^* = \frac{16\pi V_m^{\beta 2} \sigma^3}{3\Delta g_{ch}} \quad (8)$$

where  $V_m^{\beta}$  is the molar volume of the precipitate phase,  $\sigma$  is the interfacial energy and  $\Delta g_{ch}$  is the chemical driving force of the phase transformation. The Zeldovich factor is expressed as

$$Z = \frac{v_{at}^{\beta}}{2\pi r^{*2}} \sqrt{\frac{\sigma}{k_B T}} \quad (9)$$

where  $v_{at}^{\beta}$  is the atomic (molar) volume of the nucleating phase, and  $r^*$  is the critical radius of the precipitate, given by

$$r^* = \frac{2\sigma V_m^{\beta}}{\Delta g_{ch}} \quad (10)$$

The atomic attachment rate  $\beta^*$  is expressed as [26]

$$\beta^* = \frac{4\pi r^{*2}}{a^4} \min(D_{ij}^{\alpha} x_i^{\alpha}) \quad (11)$$

where  $a$  is the atomic jump distance, typically taken as the lattice constant of the matrix phase,  $D_{ij}^{\alpha}$  is the interdiffusion coefficient between the matrix and the precipitated phase, and  $x_i^{\alpha}$  is the molar fraction of component  $i$  in the matrix phase. The index  $j$  refers to the reference component with respect to which the interdiffusion fluxes are defined. The term  $\min(D_{ij}^{\alpha} x_i^{\alpha})$  identifies the rate-limiting species in the multicomponent diffusion process — that is, the species whose effective flux is the slowest and thus controls the attachment rate.

The thermodynamic quantities in the precipitation model are evaluated using a Taylor expansion around the equilibrium state. Following the derivation in [22], the chemical driving force is expressed as

$$\Delta g_{ch} = \Delta \bar{x}^T \bar{G}^{\alpha} \Delta \bar{x}^{\infty} \quad (12)$$

where  $\bar{G}^{\alpha}$  is the Hessian of the molar Gibbs energy of the matrix phase  $\alpha$ , evaluated at equilibrium:

$$\bar{G}^{\alpha} = \left. \frac{\partial^2 G_m^{\alpha}}{\partial x_i \partial x_j} \right|_{eq} \quad (13)$$

The composition differences are defined as

$$\Delta \bar{x} = \bar{x}^{\beta} - \bar{x}^{\alpha} \quad (14)$$

$$\Delta \bar{x}^{\infty} = \bar{x}^{\infty} - \bar{x}^{\beta} \quad (15)$$

where  $\bar{x}^{\alpha}$  and  $\bar{x}^{\beta}$  are the molar fractions of each species in the matrix phase  $\alpha$  and the precipitate phase  $\beta$  at equilibrium, respectively, and  $\bar{x}^{\infty}$  is the molar fraction in the matrix phase far from the precipitate.

The growth of precipitates is determined by the diffusion-limited growth rate, given by [22]

$$v(r) = \frac{1}{r \Delta \bar{x}^T \bar{M}^{-1} \Delta \bar{x}} \left[ \Delta g_{ch} - \frac{2\sigma V_m^{\beta}}{r} \right] \quad (16)$$

where  $r$  is the precipitate radius, and  $\bar{M}$  is the mobility matrix, related to the interdiffusion matrix by  $\bar{M} = \bar{D}^\alpha (\bar{G}^\alpha)^{-1}$ . As the precipitate grows, the molar fraction at the precipitate–matrix interface is altered by the Gibbs-Thomson effect and thus becomes size-dependent. The molar fraction at the precipitate side of the interface is expressed as [23]

$$\bar{x}^\beta(r) = \bar{x}^\beta(r) + \bar{G}^{\beta-1} \bar{G}^\alpha \left( \Delta \bar{x}^\infty - \frac{1}{\Delta \bar{x}^T \bar{M}^{-1} \Delta \bar{x}} \left[ \Delta g_{ch} - \frac{2\sigma V_m^\beta}{r} \right] \right) \quad (17)$$

where

$$\bar{G}^\beta = \frac{\partial^2 G_m^\beta}{\partial x_i \partial x_j} \Big|_{eq} \quad (18)$$

is the Hessian of the molar Gibbs energy of the precipitate phase  $\beta$ , evaluated at equilibrium.

#### 4.1. Coupling with Calphad thermodynamic and diffusion data

The precipitation model requires evaluation of the Hessian matrices  $\bar{G}^\alpha$  and  $\bar{G}^\beta$ , the interdiffusion matrix  $\bar{D}^\alpha$ , and the molar fraction of the phases at equilibrium  $\bar{x}^\alpha$  and  $\bar{x}^\beta$  as functions of temperature. The Haynes 282 alloy consists of ten elements in total, but not all of them contribute to the formation of the  $\gamma'$  precipitates, which are commonly described stoichiometrically as Ni<sub>3</sub>(Al, Ti). To simplify the model, the alloy is therefore approximated as a ternary Ni–Ti–Al system, chosen such that the calculated equilibrium phase fractions of the full alloy and the reduced ternary alloy match. The nominal composition of the Haynes 282 alloy and the simplified ternary composition are presented in Table 2.

The Hessian matrices are determined using finite difference and Calphad thermodynamic descriptions of the Gibbs energy. The thermodynamic and diffusion data was calculated using the Thermo-Calc Software TCS Ni-based Superalloys Database version 11 for the temperature range of  $600^\circ\text{C} \leq T \leq 1000^\circ\text{C}$  with a step of  $20^\circ\text{C}$  in the composition range of  $0 \leq x_{\text{Al}} \leq 0.4$ ,  $0 \leq x_{\text{Ti}} \leq 0.4$  with a step size of 0.5 % for both the matrix phase and precipitated phase.

The components of the interdiffusion matrix  $\bar{D}^\alpha$  are critical for accurately modeling the growth of the  $\gamma'$  phase. This process involves not only the diffusion of Ti and Al in the matrix toward the precipitate, but also the diffusion of Cr in the matrix away from the precipitate [7]. Based on this, the diffusion coefficients of Ti were extracted from Thermo-Calc in a Ni–Cr matrix with the composition Ni(80-x) at.%–Cr20 at.%–Ti  $x$  at.%, where  $x$  was varied in steps of 0.5 at.%. Similarly, the diffusion coefficients of Al were extracted in a Ni–Cr matrix with the composition Ni(80-x) at.%–Cr20 at.%–Al $x$  at.%, where  $x$  was also varied in steps of 0.5 at.%. In both cases, the data were obtained from Thermo-Calc at temperature intervals of  $20^\circ\text{C}$ .

The remaining material parameters required are the atomic jump distance, the interfacial energy, the atomic volumes of the precipitate and matrix phases, the number of nucleation sites per unit volume, and the equilibrium molar fractions. The atomic jump distance is taken as the lattice constant of the matrix phase and is estimated from the atomic molar volume by assuming an fcc structure, such that  $a^3 = 4v_{at}^\alpha$ . The atomic molar volumes for the matrix and precipitate phases were exported from Thermo-Calc as functions of temperature and composition with resolution steps of  $20^\circ\text{C}$  and 0.5 at.% in the composition range of  $0 \leq x_{\text{Al}} \leq 0.4$ ,  $0 \leq x_{\text{Ti}} \leq 0.4$ . The number of nucleation sites per unit volume is assumed to be  $N_0 = (v_{at}^\beta)^{-1}$ , i.e. equal to the atomic number density of the precipitate phase. The equilibrium molar fractions  $\bar{x}^\alpha$  and  $\bar{x}^\beta$  were obtained in steps of  $10^\circ\text{C}$  using the approximated composition given in Table 2.

The last parameter is the interfacial energy. It is taken as a constant value of  $\sigma = 0.015 \text{ J m}^{-2}$  in this work. Mukherjee et al. [7] reported  $\sigma = 0.012 \text{ J m}^{-2}$  for an ageing temperature of  $760^\circ\text{C}$ , but much higher value ( $\sigma > 0.1 \text{ J m}^{-2}$ ) for a temperature of  $650^\circ\text{C}$ . Fahrman and Metzler [27] used a constant interfacial energy of  $0.020 \text{ J m}^{-2}$  in their TC-PRISMA<sup>®</sup> based precipitation modeling over the range  $704\text{--}1093^\circ\text{C}$ . Thus, reported literature values lie in the same order of magnitude as the value used here, although interfacial energies are known to vary with composition, orientation, and temperature.

**Table 2**

The nominal composition and the ternary approximation in of Haynes 282 (at.%).

	Ni	Cr	Co	Mo	Ti	Al	Fe	Mn	Si	C
Full	56	22.2	9.8	5.1	2.5	3.2	0.7	0.1	0.2	0.3
Ternary	89.3	–	–	–	5	5.7	–	–	–	–

#### 4.2. Implementation

Following Myhr and Grong [28], the precipitate evolution is computed using a numerical Kampmann-Wagner scheme, in which the precipitate size distribution is subdivided into size classes with an associated number density of precipitates. The flux of precipitates between neighboring size classes is calculated using the growth rate of each size class. Following this approach, the precipitate number density  $N_{k,t+\Delta t}$  (number of precipitates per unit volume) of each size class  $k$  for each time step  $\Delta t$  is solved using

$$N_{k,t+\Delta t} = N_{k,t} + \frac{\Delta t}{\Delta r_k} [v_k [H(v_k)N_{k-1,t} + H(-v_k)N_{k,t}] - v_{k+1} [H(v_{k+1})N_{k,t} + H(-v_{k+1})N_{k+1,t}]] \quad (19)$$

where  $\Delta r_k$  and  $v_k$  is the width and growth rate of each size class, respectively, and  $H(x)$  is the Heaviside step function (1 if  $x > 0$  and 0 otherwise).  $N_{k,t}$  denotes the precipitate number density of size class  $k$  from the previous time step. Once the precipitate size distribution is updated, the matrix composition is calculated using mass conservation of all elements

$$x_i^\alpha(1-f) = x_i^\infty - f_i^\beta \quad (20)$$

where  $f = 4\pi/3 \sum_k N_k r_k^3$  is the volume fraction of precipitates,  $x_i^\infty$  is the initial molar fraction and  $f_i^\beta = \sum_k \bar{x}_{i,k}^\beta N_k r_k^3$  is the average precipitate molar fraction of element  $i$ , where

$$\bar{x}_{i,k}^\beta = \frac{3}{r_k^3} \sum_k x_i^\beta(r_k) r_k^2 \Delta r_k \quad (21)$$

and  $x_i^\beta(r_k)$  is given by Eq. (17).

To ensure numerical stability, precipitates are forced not to move more than one size class in each time step, providing the following constraint [29]

$$\Delta t < \min \left( \frac{\Delta r_k}{|v_k|} \right) \quad (22)$$

By combining the Kampmann-Wagner scheme with the models for the nucleation and growth rate described in Section 4, the evolution in the distribution of the precipitate density, the volume fraction and the changes in the composition of the matrix can be calculated. The scheme is implemented as a subroutine to the FE program and is solved for each node after a converged time step of the thermal model. The scheme is summarized as follows:

For each converged thermal solution  $T_n$  in FE model, for each node:

If  $T_l \leq T_n \leq T_{max}$  then solve the CNGT model between  $T_{n-1}$  and  $T_n$  using linear interpolation and substepping. The temperature history for the precipitation model is approximated to be  $T_n = T_{n-1} + \Delta T_m + \Delta T_{m+1} + \dots$  where  $\Delta T_m$  is the temperature increment of precipitation-substep  $m$  determined from the substep time increment  $\Delta t_m$  (see Eq. (22)). For each substep  $m$ , do:

1. Interpolate  $\bar{G}^\alpha$ ,  $\bar{G}^\beta$ ,  $\bar{D}^\alpha$ ,  $\bar{x}^\alpha$  and  $\bar{x}^\beta$  with respect to the temperature and matrix molar fraction from the tabulated data.
2. Evaluate the chemical driving force  $\Delta g_{ch}$  and compute the nucleation rate and the growth rate using Eqs. (7) and (16), respectively. Use the growth rate together with Eq. (22) to determine the substep time  $\Delta t_m$ , obtain the corresponding temperature increment  $\Delta T_m$  by linear interpolation between  $T_{n-1}$  and  $T_n$ .

3. Insert the number of new nuclei  $\Delta N = (1 - f)I\Delta t_m$  in  $r = r^* + 0.5\sqrt{k_B T / \pi \sigma}$  [29] and update the size distribution using the growth rate and numerical update scheme Eq. (19).
4. Compute the transformed volume fraction, determine the average precipitate molar fraction, and update the matrix composition using Eq. (20).
5. Repeat steps 1–4 until the temperature in the precipitation model reaches  $T_n$ .

The simulations are initiated with  $N_{k,t=0} = 0$  for all size classes on a grid consisting of 300 size classes ranging from  $r = 0.1$  nm to  $r = 300$  nm. To reduce computational cost, the size classes are represented on a logarithmic grid. This weights the discretization to the nano-sized regime where a finer grid is required because of the high growth rate and also reduces the total number of grid points. Additionally, precipitates contained in size classes with  $r < 0.5r^*$  are removed from the size distribution because these particles are smaller than the critical size and are assumed to dissolve.

The thermal FE model into which the material model is implemented does not account for highly non-equilibrium solidification phenomena such as solute trapping, rapid interface motion, or ultrafast thermal transients in the melt pool. In this work, we assume that these effects primarily influence the solidification microstructure and the initial micro-segregation, rather than the  $\gamma'$  phase formation. The  $\gamma'$  precipitates form predominantly during the repeated reheating and cooling cycles that occur after solidification, when additional layers are deposited. Moreover, the purpose of applying CNT here is to estimate relative nucleation tendencies and trends, rather than to reproduce the complete kinetic pathways under far-from-equilibrium conditions.

## 5. Results and discussions

In the following, the precipitation evolution obtained from the FE simulations using the CNGT model is compared with experimental findings from the SAXS/WAXS and APT measurements. In addition, results from the calibration of the heat source are presented.

### 5.1. Finite element model calibration

The heat transfer coefficient in the fixture clamps,  $h_{\text{fix}}$ , and the laser efficiency coefficient,  $\eta$ , were calibrated so that the simulated temperatures matched the measured values. The cooling times between turned off during the experiment. The calibrated values were found to be  $h_{\text{fix}} = 850 \text{ W m}^{-2} \text{ K}^{-1}$  and  $\eta = 0.45$  and is in the same order as in [21]. The simulated temperature histories, extracted from node points corresponding to the thermocouple locations, are shown in Fig. 5 alongside the experimental data. The parameters of the boundary conditions are presented in Table 3.

We acknowledge that thermocouple measurements do not capture the exact temperature in the immediate laser-feedstock interaction zone due to spatial separation and time delay in the thermal response. However, the measured temperatures effectively reflect the overall energy absorbed by the workpiece and the subsequent heat transfer, including conduction through the build and plate, as well as convective and radiative losses. Consequently, the boundary conditions implemented in the simulation, which account for these heat transfer mechanisms, provide a realistic approximation of the thermal history throughout the build, as can be seen by the high correlation between the simulation and the experiment in both measurement points. While local melt pool temperatures may differ, the simulated temperature fields are expected to accurately capture the thermal conditions relevant for simulating the  $\gamma'$  precipitation during the manufacturing process.

**Table 3**

Parameters for the thermal boundary conditions and the heat source.

$h_{\text{fix}}$ ( $\text{W m}^{-2} \text{ K}^{-1}$ )	$h_{\text{air}}$ ( $\text{W m}^{-2} \text{ K}^{-1}$ )	$T_{\infty}$ ( $^{\circ}\text{C}$ )	$\epsilon$ (–)		
850	15	25	0.2		
$\eta$ (–)	$P$ (W)	$a_f$ (mm)	$a_r$ (mm)	$b$ (mm)	$c$ (mm)
0.45	3000	2	4	2	3

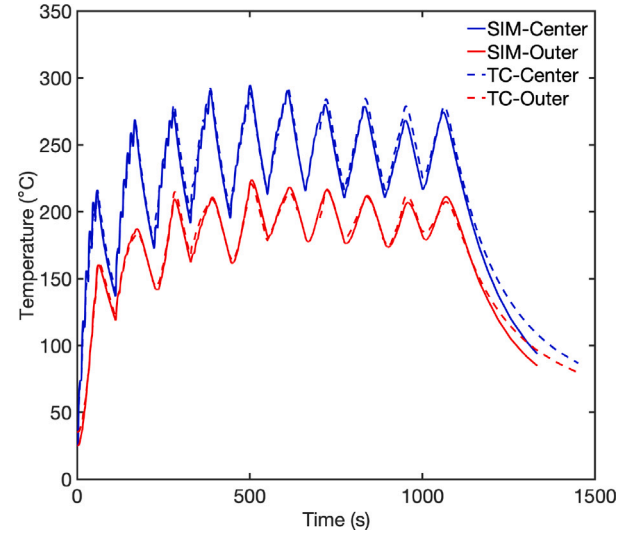


**Fig. 5.** Simulated temperature history at the thermocouple positions and the measured values from the experiment described in Section 2.

### 5.2. Simulated precipitate size in sample no. 1

To demonstrate the functionality of the precipitation model, the temperature history was extracted from the FE simulation at the center of the build (5.5 mm above the build plate, at the same horizontal and vertical position as the central thermocouple). To improve computational efficiency, the model was limited to nucleation and growth within the temperature range  $600^{\circ}\text{C} < T < 950^{\circ}\text{C}$ , and only this range is displayed. This interval was chosen because the  $\gamma'$  phase is no longer stable above  $950^{\circ}\text{C}$ , according to Thermo-Calc simulations. This temperature is however below to the  $\gamma'$  solvus temperature of  $997^{\circ}\text{C}$  reported by Haynes International [30], but it is assumed that this discrepancy will not affect the final result. At  $600^{\circ}\text{C}$ , the diffusion of Al in Ni is approximately 1000 times slower than at the ageing temperature of  $788^{\circ}\text{C}$ , while the diffusion of Ti is about 550 times slower. Based on this, diffusion is considered too sluggish to enable significant precipitate growth. The results from the CNGT model, based on the extracted temperature data, are shown in Fig. 6. They indicate that precipitates form and dissolve repeatedly throughout the process, eventually stabilizing at a radius slightly larger than 1 nm, with a final volume fraction of approximately 1%.

The CNGT model has been implemented as described in Section 4.2, and Fig. 7 presents the FE simulated mean particle radius and number density of the  $\gamma'$  precipitates formed during the building process. The number density is on the order of  $10^{24} \text{ m}^{-3}$ , and the mean precipitate radius is approximately 1 – 2 nm. These results demonstrate that the driving force for nucleation is large in Haynes 282. The rapid nucleation of precipitates aligns with previous experimental findings for this alloy, where precipitates were observed in samples that had been solution heat-treated at  $1010^{\circ}\text{C}$  for 2 h in a vacuum furnace, followed by convection cooling in argon [9].

Fig. 7(c) shows the variation in precipitate radius, while Fig. 7(d) shows the variation in number density, both taken from a cross-section through the longitudinal center of the sample. The results indicate that

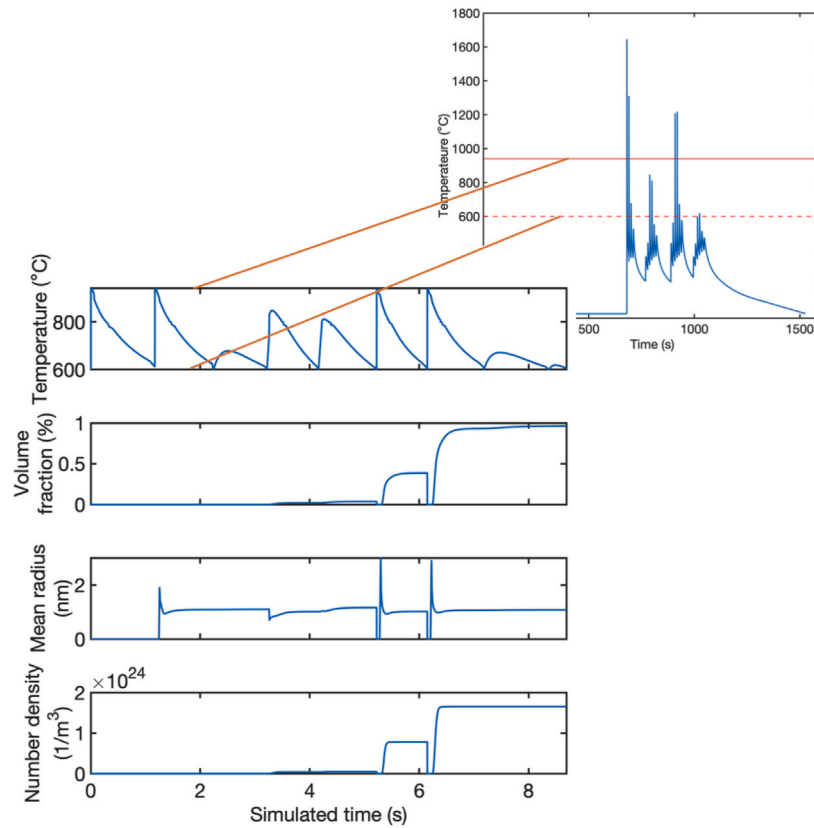


**Fig. 6.** Precipitation of  $\gamma'$  precipitates during the manufacturing process. The simulated time represents the time the temperature has been within the range  $600^\circ\text{C} < T < 950^\circ\text{C}$ .

the microstructure is relatively homogeneous, with variations only at the edges of the build and in the very first and last layers. This may be due to the simple geometry. For more complex geometries with a more intricate thermal history, larger variations may be observed.

### 5.3. Precipitate size from synchrotron measurements in sample no. 1

To verify the precipitate modeling strategy and its implementation in the FE software, combined SAXS and WAXS measurements were performed as a line scan on a 2 mm thick sample taken from the center of the build. SAXS is a technique by which scattering length density differences in a sample can be quantified and is a common method for measuring precipitate size and its distributions in metallic systems. WAXS relies, on the other hand, on structural ordering of the atoms and a combination of SAXS and WAXS make it possible to detect the size distribution of precipitates and phases that are present in the measurement point.

Fig. 8(a) presents the 2D SAXS pattern from sample no. 1, obtained after integrating the raw data using the pyFAI library [31], where several distinct streaks are visible. In the literature, streaks in SAXS patterns have been attributed to various origins: aligned precipitates [32, 33], possible double Bragg reflections within a single grain [34], or ordered dislocations [35]. For double Bragg reflections to affect a SAXS pattern, a strongly textured, large-grained material is required [36]. Unlike in strongly textured, large-grained materials, our measurements probe a polycrystalline volume with many randomly oriented grains, which averages out potential double Bragg effects. Therefore, it is reasonable to neglect double Bragg reflections. In the subsequent analysis, the main streaks are attributed either to dislocations or to aligned precipitates.

To analyze the anisotropic behavior of the SAXS pattern, the variation of intensity for three different  $q$ -ranges as a function of the

azimuthal angle is shown in Fig. 8(b). The intensity shows a symmetric behavior with angular separation of approximately  $90^\circ$  between the large peaks, and  $45^\circ$  shifted smaller peaks. The amplitude of the streaks attenuates with the  $q$ -range. A more detailed discussion will follow in the end of this section.

Over the years, several methodologies have been developed to extract physical parameters from SAXS measurements where one method is to fit a function to the experimental data that describes the relationship between the measured differential scattering cross section and the distribution of scattering length density in the sample [37]. Assuming a polydisperse particle size distribution  $D(r, \sigma, \mu)$  and that the precipitates are spherical, we end up with [38,39]

$$I(q) = N(\Delta\rho)^2 \int_0^\infty D(r, \sigma, \mu) [V_p F(q, r)]^2 dr + c_0 + c_1 q^{-c_2} \quad (23)$$

where  $N$  is the precipitate number density ( $\text{m}^{-3}$ ),  $\Delta\rho$  is the difference in scattering length density between the matrix and the precipitate, and  $F(q, r)$  is the form factor of a particle with radius  $r$  and volume  $V_p(r)$  with a scattering vector  $q = |\vec{q}|$ . The form factor of a spheroid is given in [39]. For a random nucleation and growth process, a log-normal size distribution is often a suitable choice [40,41].

The intensity model in Eq. (23) assumes one particle size distribution. However, objects that are outside the measured  $q$ -range, or other objects that the single distribution intensity model does not directly account for, may contribute to the scattered intensity. The scattering from these precipitates must be included in the model and, therefore, the background term  $c_1 q^{-c_2}$  has been included [9]. The  $q$ -independent background term  $c_0$  takes into account fluorescence scattering as well as air scattering.

To investigate the streaks observed in the SAXS intensity data, integrated azimuthal angle intervals of  $\chi = 10^\circ - 65^\circ$ ,  $\chi = 65^\circ - 105^\circ$ , and  $\chi = 105^\circ - 160^\circ$  were used to extract parameters from the model describing the distribution of scattering length density in the sample, Eq. (23).

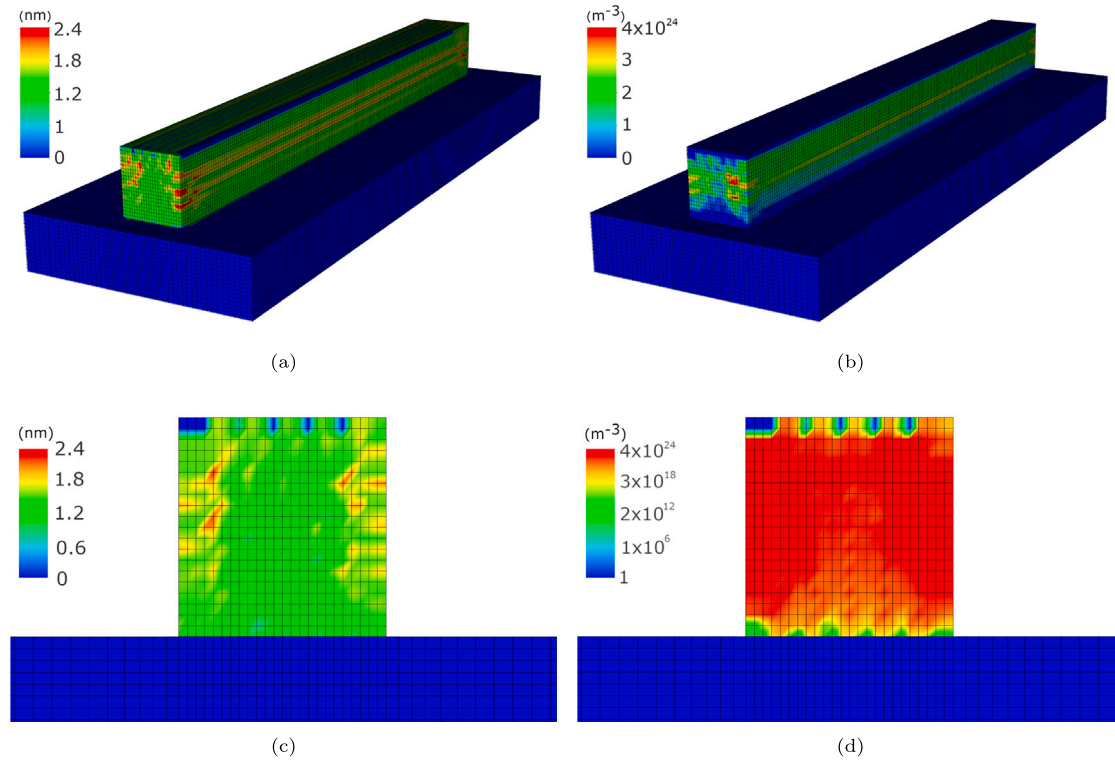


**Fig. 7.** Modeled precipitate radius and number density. (a) Precipitate size (nm), (b) number density ( $\text{m}^{-3}$ ), (c) precipitate radius shown as a cross-section taken from the center of the sample, and (d) the number density presented on a logarithmic scale.

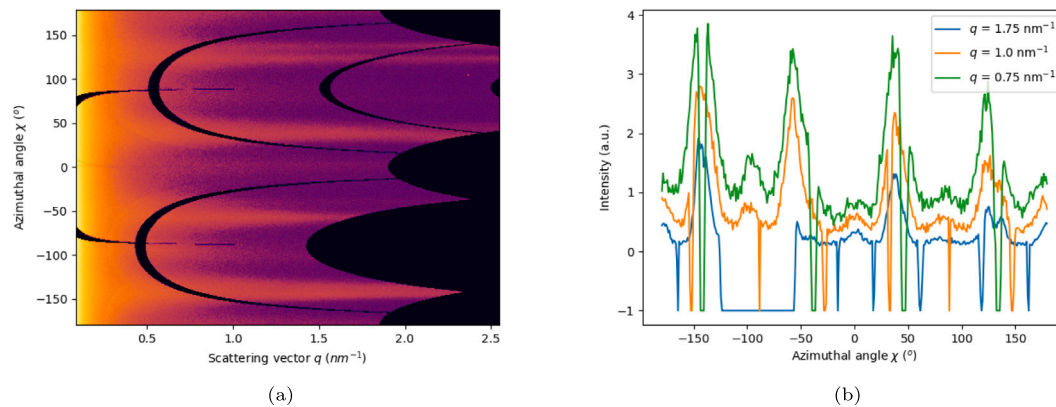


**Fig. 8.** SAXS data from sample nr 1. (a) Azimuthally integrated data. The strikes originates probably from aligned precipitates or from ordered dislocations. (b) Intensity variations originating from three different  $q$ -values.

The parameters were obtained by minimizing the error between the intensity model, Eq. (23), and the measured intensity using Python and the `least_squares` routine from the SciPy optimization toolbox similarly as described in [9]. However, during the fitting process, the linear and non-linear terms were separated [39]. To extract the number density, a scattering length density contrast of  $\Delta\rho = 6 \cdot 10^{-6} \text{ nm}^{-2}$  was assumed, based on the compositional difference between the matrix and the precipitates.

For the interval  $\chi = 10^\circ\text{--}65^\circ$ , no physically reasonable parameters could be determined. This is in contrast to the intervals  $\chi = 65^\circ\text{--}105^\circ$  and  $\chi = 105^\circ\text{--}160^\circ$ , where a mean particle radius of approximately  $r = 1 \text{ nm}$  and a number density of  $N \approx 1 \cdot 10^{24} \text{ m}^{-3}$  could be obtained, depending on the measurement position, see Fig. 9. Comparison of the experimental data with the results from the CNGT model shows that the model accurately predicts both the number density and the mean particle radius.

The azimuthally integrated WAXS diffraction data from sample no. 1 are presented in Fig. 10(a). The data reveal intense peaks corresponding to the  $\gamma$  phase, along with several weaker peaks corresponding to the metallic carbide MC phase ( $M = \text{Ti}, \text{Mo}$ ). Other carbides typically observed in Haynes 282, such as  $\text{M}_{23}\text{C}_6$  and  $\text{M}_6\text{C}$  [5], are not detected in the diffraction data. No isolated diffraction peaks originating from the  $\gamma'$  phase are observed, such as the (211) peak. However, other  $\gamma'$  peaks, such as the (111) or (200), coincide with the  $\gamma$  phase peak positions, making them indistinguishable. See e.g. [9].

Fully integrated WAXS data can obscure weak Bragg peaks originating from the  $\gamma'$  phase due to background noise. The diffraction data was therefore integrated in angular sections, so called caking, to minimize the effect of background noise. Fig. 10(b) shows sectional integration of the diffraction pattern in the  $q$ -range of  $36\text{--}46 \text{ nm}^{-1}$ , which is in the range where we expect a single peak originating from the  $\gamma'$  phase. For an angle of  $90 \pm 11^\circ$ , one can clearly see a diffraction peak originating

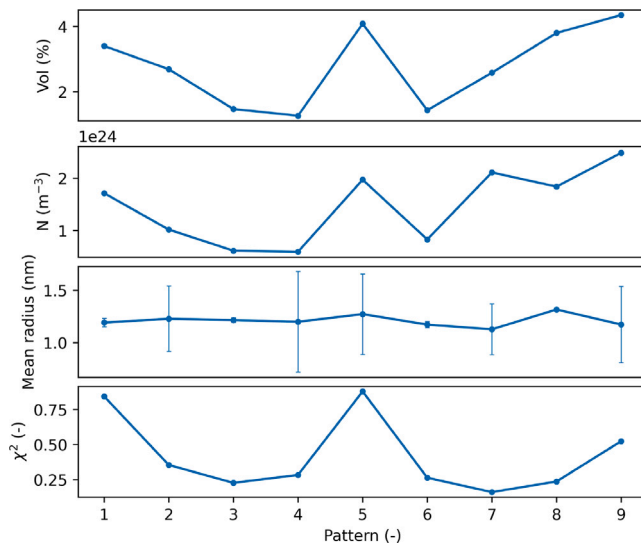


**Fig. 9.** Extracted parameters from the SAXS intensity curves obtained from the as-built sample no. 1. From top to bottom: the precipitate volume fraction, the number density, the mean particle radius, and the chi-squared parameter, which indicates the quality of the fit between the model and the experimental data. The uncertainties for the number density and the mean radius have been extracted from the fitting process using diagonal elements of the covariance matrix obtained from the least-squares fitting process. For the number density, the uncertainties have a maximum value of  $N = \pm 3 \cdot 10^{22} \text{ m}^{-3}$ . The volume fraction is calculated from the number density and the mean particle radius. Each data point corresponds to a horizontal measurement position located 5.5 mm above the build plate, with a step size of 1 mm.

from the  $\gamma'$  phase. This indicates that the  $\gamma'$  phase is not randomly oriented.

#### 5.4. Atom probe tomography of sample no. 1

To investigate the nanoscale structure of the as-built material, APT measurements were performed on a lamella lifted from the center of the build, approximately 5 mm above the build plate and 1 mm from the edge, as shown in Fig. 7.

The reconstructed data revealed a non-uniform distribution of  $\gamma'$  precipitates, forming ring-shaped patterns as shown in Fig. 11. To verify the presence of the  $\gamma'$  phase and distinguish genuine clustering from random fluctuations, the radial distribution function has been utilized to determine the amplitude and extent of concentration fluctuations. The results revealed a 50/50 concentration ratio between Al and Ti, with a domain size of approximately 2 nm, as shown in Fig. 12(a).

To provide further insights into the size and composition of the precipitates, iso-concentration surfaces are applied to characterize the  $\gamma'$  phase, defined by an Al and Ti concentration surface of 10 at.% with a threshold confidence of 0.1. The 10 at.% (Al + Ti) iso-concentration threshold was selected based on proxigram analysis, where it corresponds to an intermediate concentration between the matrix ( $\approx 5.7$  at.%) and the precipitate core, thereby providing a robust and reproducible definition of the  $\gamma'$ -matrix interface. A noise filter was applied to remove any surface areas smaller than 25 facets. Proxigrams were created in the normal direction of the iso-surface with a bin size of 0.1 nm, as shown in Fig. 12(b).

The noise filtered precipitates are exported on the higher gradient side of the iso-surface to obtain their average radius excluding 15 % of the top and bottom extreme values. Thus, the average size of  $\gamma'$  is  $r = 1.90 \pm 0.42 \text{ nm}$ , assuming the precipitates are spherical. The number density  $N \approx 5 \cdot 10^{22} \text{ m}^{-3}$  is calculated based on the volume of the reconstructed tip and identified precipitates within it as displayed in

**Table 4**  
Composition of  $\gamma'$  precipitates.

	Ni	Al	Ti	Co	Cr
Composition (at.%)	58.8	10.8	11.4	8.0	7.8
Error (at.%)	0.8	0.4	0.6	0.4	0.3

**Fig. 11.** The volume fraction is calculated using the lever rule based on Al-compositions as,  $V_f = (C_n - C_m)/(C_p - C_m)$ . Where  $C_n$  is the nominal composition,  $C_m$  is the matrix composition and  $C_p$  is the precipitate composition. From the calculations we obtain a  $\gamma'$  volume fraction of approximately 2 %.

The composition of  $\gamma'$  has been further analyzed and obtained from the proxigram. The results are presented in Table 4. It is worth noticing that the precipitates contain significant amounts of Co and Cr. The Co concentration in the precipitates are close to the nominal value while they are significantly depleted in Cr, see Table 2. These observations are consistent with previously reported values [7].

Although Co and Cr are detected within the  $\gamma'$  precipitates, both elements are known to substitute predominantly on the Ni sublattice of the L1<sub>2</sub> structure without altering the crystal structure or the fundamental phase identity [42]. In the present work, a simplified compositional description of  $\gamma'$  can therefore be adopted in order to focus on the dominant thermodynamic and kinetic mechanisms governing precipitation. This choice avoids the added uncertainty that can arise when modeling highly multicomponent systems with limited thermodynamic data availability.

Within this modeling framework,  $\gamma'$  nucleation is primarily determined by the chemical driving force, whereas subsequent particle growth is controlled by atomic mobilities. The effect of the principal alloying elements on diffusion kinetics is included through composition-dependent interdiffusivity matrices, represented by Ni-Cr-Al for Al diffusion and Ni-Cr-Ti for Ti diffusion. In this manner, the kinetic influence of the major alloying constituents is retained, even though Co and Cr are not explicitly treated as  $\gamma'$ -forming species.

#### 5.5. Precipitate size in samples no. 2 and no. 3

From the results in the previous sections, we can conclude that there are  $\gamma'$ -precipitates forming during the manufacturing process. To investigate how these nuclei influence the microstructure in an ageing heat treatment process, two different heat treatment processes were utilized. Sample no. 2 underwent an ageing heat treatment at 788 °C for 8 h directly after the manufacturing process, whereas sample no. 3 was first solution heat treated at 1120 °C for 2 h and then slowly cooled down to room temperature. After that, it was heat treated at 1010 °C for 2 h, before it was slowly cooled down and age heat treated at 788 °C for 8 h. The cooling rate is estimated to be 20–25 °C min<sup>-1</sup>.

To assess if the heat treatments induce any variations in the existing phases, the WAXS patterns of samples no. 2 and no. 3 are compared with each other. The diffraction patterns are shown in Fig. 13. From the results, it is seen that there are only minor variations in the diffraction data, concluding that there are no variations in present phases. Note that during the heat treatments, the M<sub>23</sub>C<sub>6</sub> phase is formed, but the MC phase is present already from the building process (see Fig. 10(a)).

The  $\gamma'$  precipitate size distributions for sample no. 2 and sample no. 3 were experimentally determined by fitting the scattering length density model, Eq. (23), to azimuthally integrated SAXS intensity data. As a high volume fraction of precipitates is expected, a structure factor was included in the model as well [43]. The results of the minimization process are presented in Fig. 14, where it can be clearly seen that the particle radius differs significantly depending on the heat treatment ( $r \approx 11.5 \text{ nm}$  for sample no. 2 and  $r \approx 15 \text{ nm}$  for sample no. 3). These values are within the size range previously reported for standard ageing heat treatments of this alloy and manufacturing process [4]. The extracted precipitate volume fraction, number density, width of the size

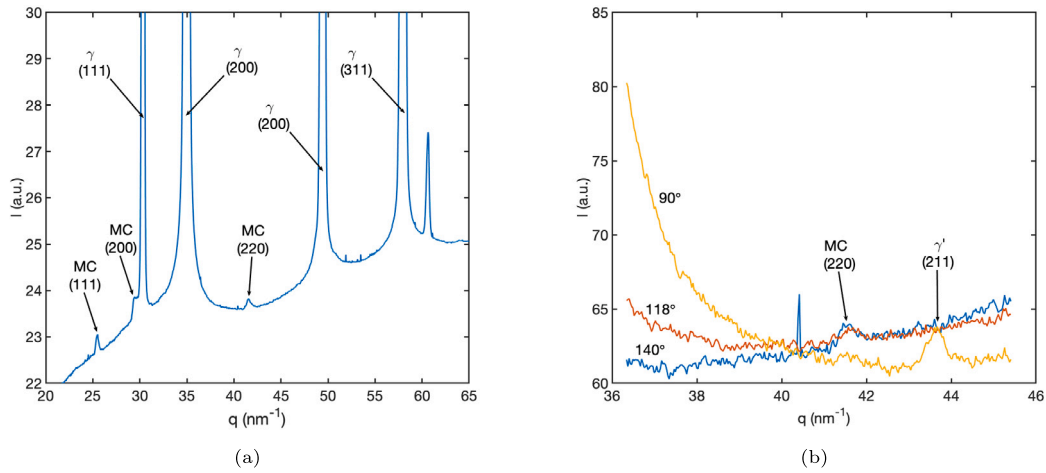


Fig. 10. Azimuthally integrated diffraction data originating from sample no. 1. (a) The data is fully azimuthally integrated, and in (b) the data has been sectionally integrated.

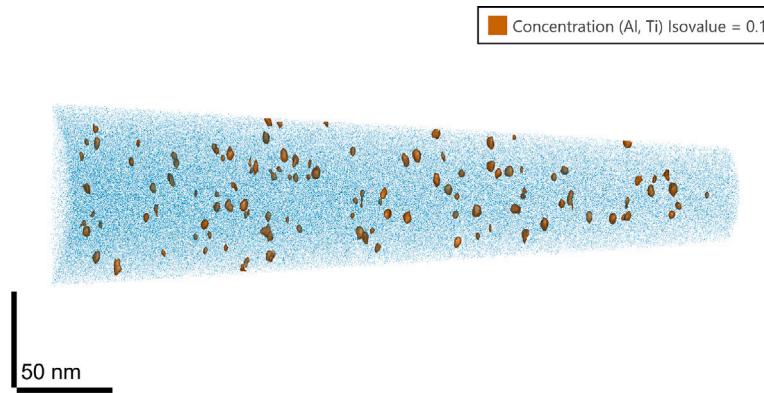


Fig. 11. Blue Ni atoms, orange-brown surface = 10 at.% (Al, Ti), total volume 59.6 million ions.

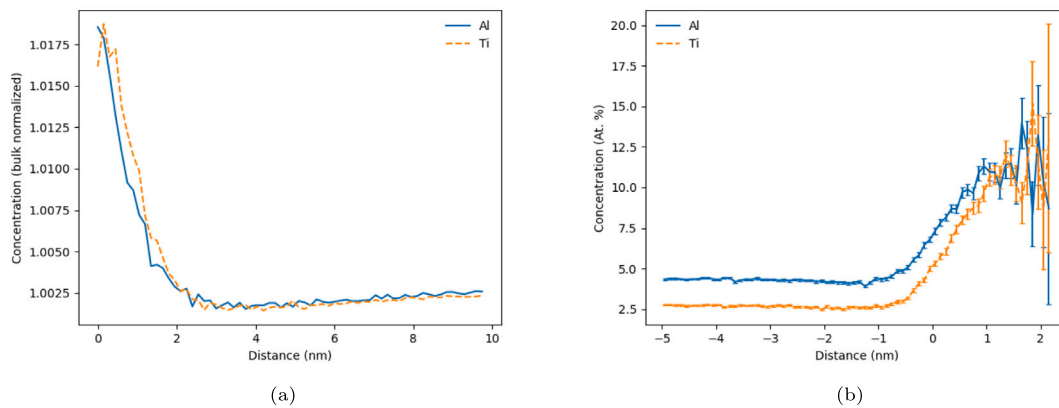


Fig. 12. (a) Bulk-normalized radial distribution function (RDF) of Ti and Al ions. (b) Proxigram of the Al and Ti concentration profiles measured normal to the iso-concentration surface defined by an Al + Ti threshold of 10 at.%, where 0 distance corresponds to the iso-surface location.

distribution, as well as the mean radius, are presented in Fig. 15. The particle number density and particle volume fraction are also within the expected range compared to previously reported results for this alloy [9].

Based on the SAXS results it is not possible to conclude whether the larger precipitate size distribution originates from the AM process or from variations in the heat treatment (remember that sample no. 3 was first heat treated at 1010 °C before it was cooled down to the ageing temperature 788 °C, which is not the case for sample no. 2 where the

ageing process started at room temperature). However, three various heat treatments can be modeled applying the CNGT. Therefore, three temperature scenarios have been used to simulate the precipitate size distribution:

- The first scenario involves a heat treatment for 8 h at 788 °C. The temperature is assumed to increase linearly from 25 °C to 788 °C in 30 min and after the 8 h of heat treatment a linearly decrease in temperature to 25 °C in 30 min is assumed.

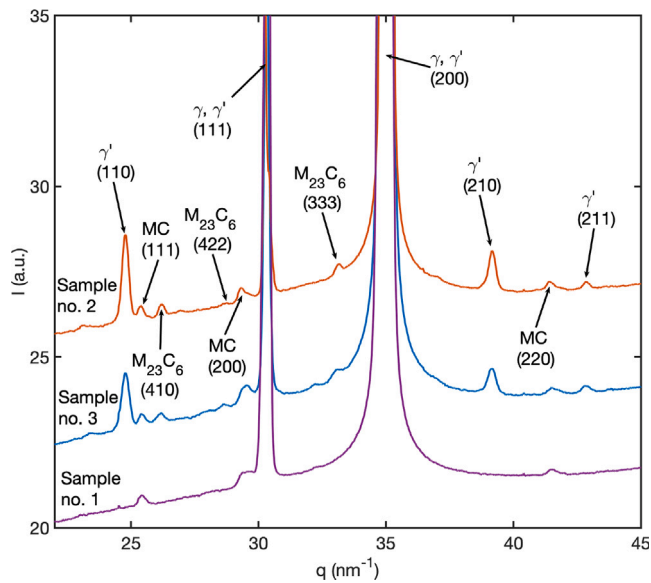


**Fig. 13.** Azimuthally integrated diffraction data originating from samples no. 2 and no. 3. No large variations in the diffraction pattern can be seen. The diffraction pattern from sample no. 1 (the same as in Fig. 10) has been included as a reference.

- The second scenario involves a heat treatment at 788 °C for 8 h, with an initial condition of a particle size distribution originating from the AM building process (FE simulated temperature history). The temperature is assumed to increase linearly from 25 °C to 788 °C in 30 min and after the 8 h of heat treatment a linearly decrease in temperature to 25 °C in 30 min is assumed. This correspond to sample no. 2.
- The third scenario comprises a heat treatment starting at 1010 °C followed by a linear decrease to 788 °C within 30 min. Subsequently, an ageing heat treatment at 788 °C for 8 h is applied, followed by a cooling to 25 °C in 30 min. This correspond to sample no. 3.

Fig. 16 shows the results from the three heat treatment scenarios. The precipitate size distribution exhibits a larger mean radius for the sample subjected to the third heat treatment scenario (sample no. 3) compared to the other two scenarios. Interestingly, no significant variation in precipitate size is observed between heat treatment scenarios one and two. Thus, the precipitates nucleated during manufacturing do not affect the final precipitate volume fraction or size distribution. This is likely because  $\gamma'$  in Haynes 282 starts to nucleate early during the heating process, as the temperature increases from room temperature to the ageing temperature. Therefore,  $\gamma'$  nuclei that are formed during the manufacturing process play only a minor role in the final size distribution and volume fraction.

In Haynes 282, the mechanical strength and creep resistance are primarily governed by the  $\gamma'$  particle size and size distribution after ageing [4,5]. Since the  $\gamma'$  sizes obtained after ageing are comparable regardless of whether in-process precipitates are present in the as-deposited condition, rapid nucleation during manufacturing is not expected to have a significant impact on the final mechanical performance once standard ageing treatments are applied.

Comparing scenarios one and two with scenario three, it is clear that the nucleation and growth behavior of the precipitates differ significantly. In scenarios one and two, precipitate growth occurs after a peak in precipitate number density has been reached, whereas no such peak is observed in scenario three. This difference arises because the chemical driving force and the diffusivity prior to reaching the ageing temperature are markedly different. As a result, in scenario three

nucleation and growth occur mainly during cooling, while in scenarios one and two growth takes place after the number density of precipitates has decreased. Although a steady-state size distribution is not reached for scenario one and two, the heat treatment in scenario three results in a stable particle size and volume fraction that persist for an extended period during ageing.

The second and third scenarios correspond to the heat treatments applied to sample no. 2 and sample no. 3, where SAXS measurements result in a mean precipitate radius of approximately 11.5 nm with a number density of  $1.6 \cdot 10^{22} \text{ m}^{-3}$  and 15 nm with a number density of  $7 \cdot 10^{21} \text{ m}^{-3}$ , respectively. The simulated mean radius, shown in Fig. 16, are approximately 15 nm with a final number density of  $3 \cdot 10^{22} \text{ m}^{-3}$  and 20 nm with a final number density of  $7 \cdot 10^{21} \text{ m}^{-3}$ , respectively. This indicates a discrepancy with the experimental results in terms of precipitate radius, while the number densities are reproduced well. Despite these differences in absolute values, the trend is consistent: the heat treatment in scenario three produces a larger average precipitate size than that in scenario two.

The discrepancy between the measured and simulated precipitate radius may arise because the diffusion rate does not accurately capture the diffusion of alloying elements in the real material. Another parameter that can influence the final precipitate radius is the chemical driving force. In this work, we simplified the Haynes 282 alloy to a ternary system. While this may be an over-simplification, the chemical driving force strongly affects the nucleation rate and, consequently, the number of precipitates (see Eq. (7)). Nevertheless, the simulated number density agrees well with the measured number densities, both for the as-built samples and for the aged samples. This suggests that the chemical driving force is reasonably well represented in the ternary system. A final parameter known to influence the results is the surface energy. In our simulations, we apply a constant value, although in reality it depends on both temperature and the curvature (radius) of the precipitates [24].

## 6. Summary and conclusions

The mean particle size and corresponding volume fraction in a laser metal deposition (LMD) manufacturing process were simulated using the classical nucleation and growth theory (CNGT) at each node point in a finite element (FE) framework. The CNGT model utilized Calphad thermodynamic and diffusion data and the simulated precipitate sizes and volume fractions were compared with results from small- and wide-angle X-ray scattering (SAXS/WAXS) and atom probe tomography (APT).

To investigate whether precipitates nucleated during manufacturing influence the final precipice size after a standard heat treatment, the manufactured samples were directly subjected to an ageing process. The resulting  $\gamma'$  size distribution was measured using SAXS and compared with simulations assuming no initial precipitates.

In addition to the standard heat treatment, an alternative treatment was applied in which the precipitates were first dissolved at an elevated temperature, followed by gradual cooling to the final heat treatment temperature. The resulting size distribution was measured, and the precipitate evolution under the different heat treatment scenarios was compared with the simulation results.

From the results we can conclude that:

- The CNGT model has been successfully implemented as a multi-scale framework within a FE software simulating the LMD process accurately. The simulations predict the temperature history very well and it resulted in a homogeneous precipitate sizes distribution in the final LMD build, ranging from 1–2 nm with a volume fraction of approximately 1 %. These results are consistent with the SAXS measurements, which show a mean radius of  $1.2 \pm 0.5 \text{ nm}$  and a volume fraction slightly greater than 1 %.

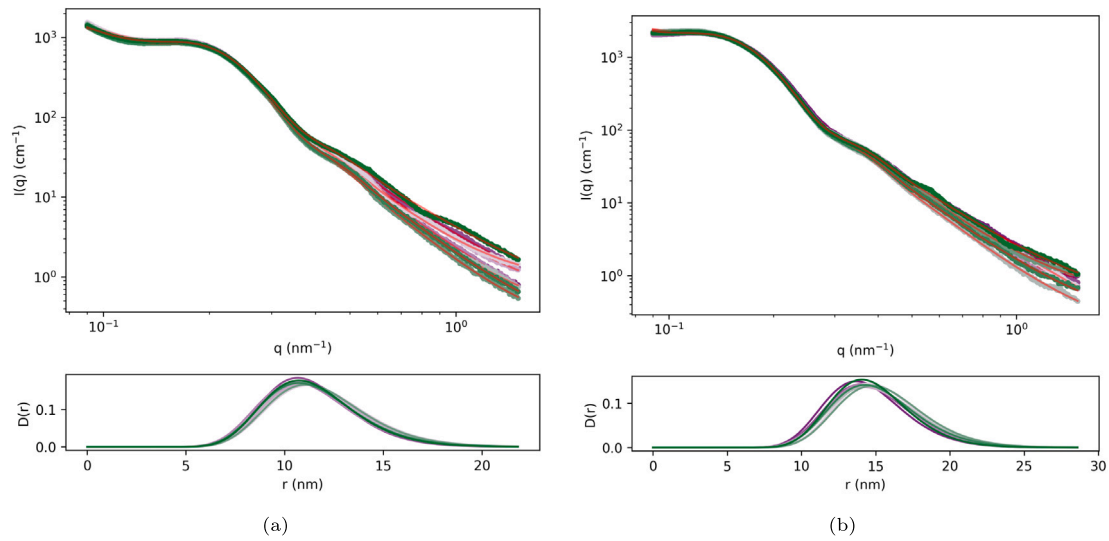


**Fig. 14.** Top: experimental and fitted intensity curves for (a) sample no. 2 and (b) for sample no. 3. Bottom: the predicted precipitate size distribution  $D(r)$ . Each line color represent a unique y-position.

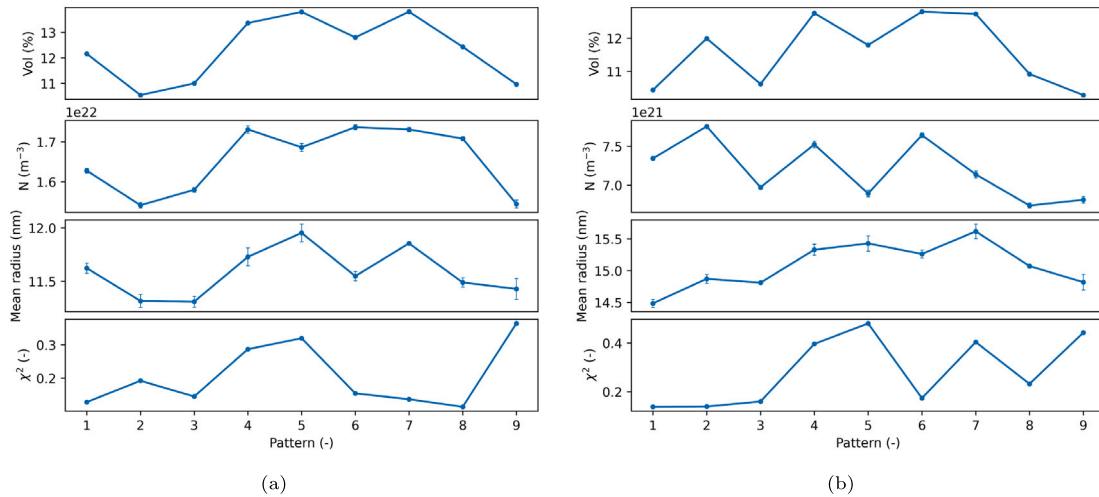


**Fig. 15.** Extracted parameters from the SAXS intensity curves for (a) sample no. 2 and (b) sample no. 3. From top to bottom: the precipitate volume fraction, the number density, the mean particle radius, and the chi-squared parameter, which indicates the quality of the fit between the model and the experimental data. The uncertainties for the number density and the mean radius have been extracted from the fitting process using diagonal elements of the covariance matrix obtained from the least-squares fitting process. For the number density, the maximum uncertainties are  $N = \pm 1 \times 10^{20} \text{ m}^{-3}$  for sample no. 2 and  $N = \pm 4 \times 10^{19} \text{ m}^{-3}$  for sample no. 3. The corresponding maximum uncertainties in the mean particle radius are  $r = \pm 0.10 \text{ nm}$  and  $r = \pm 0.12 \text{ nm}$ , respectively. The volume fraction is calculated from the number density and the mean particle radius. Each data point corresponds to a horizontal measurement position located 5.5 mm above the build plate, with a step size of 1 mm.

- The APT results show clusters of concentrated Al and Ti atoms, and by assuming a spherical shape, the average radius of the  $\gamma'$  precipitates is determined to be  $1.9 \pm 0.42 \text{ nm}$ , with a volume fraction of approximately 2 %. This is also in the same range as the simulated precipitate size and volume fraction.
- Using CNGT, the final precipitate size after the manufacturing process followed directly by an ageing process is compared with SAXS results. The simulated precipitate size shows a mean radius of approximately 15 nm with a number density of  $3 \cdot 10^{22} \text{ m}^{-3}$ , slightly larger than the radius 11.5 nm and number density  $1.6 \cdot 10^{22} \text{ m}^{-3}$  observed by SAXS. The nucleated precipitates formed during manufacturing has no significant impact on the final precipitate size or volume fraction in samples subjected to standard ageing heat treatment.
- The alternative heat treatment, in which the sample is slowly cooled from an elevated temperature, results in an increased mean particle size compared to the standard ageing process. The precipitate radius is simulated to be 20 nm with a number density of  $7 \cdot 10^{21} \text{ m}^{-3}$ . The radius is slightly larger than the measured mean radius of approximately 15 nm but the number measured number density is the same as the simulated.

The results of this work demonstrate that Calphad thermodynamic and diffusion data can be effectively used as input to simulate precipitate evolution with high accuracy using the CNGT, implemented within a multi-scale framework integrated into finite element software. This methodology provides a valuable tool for predicting microstructural variations in functionally graded components in future applications.

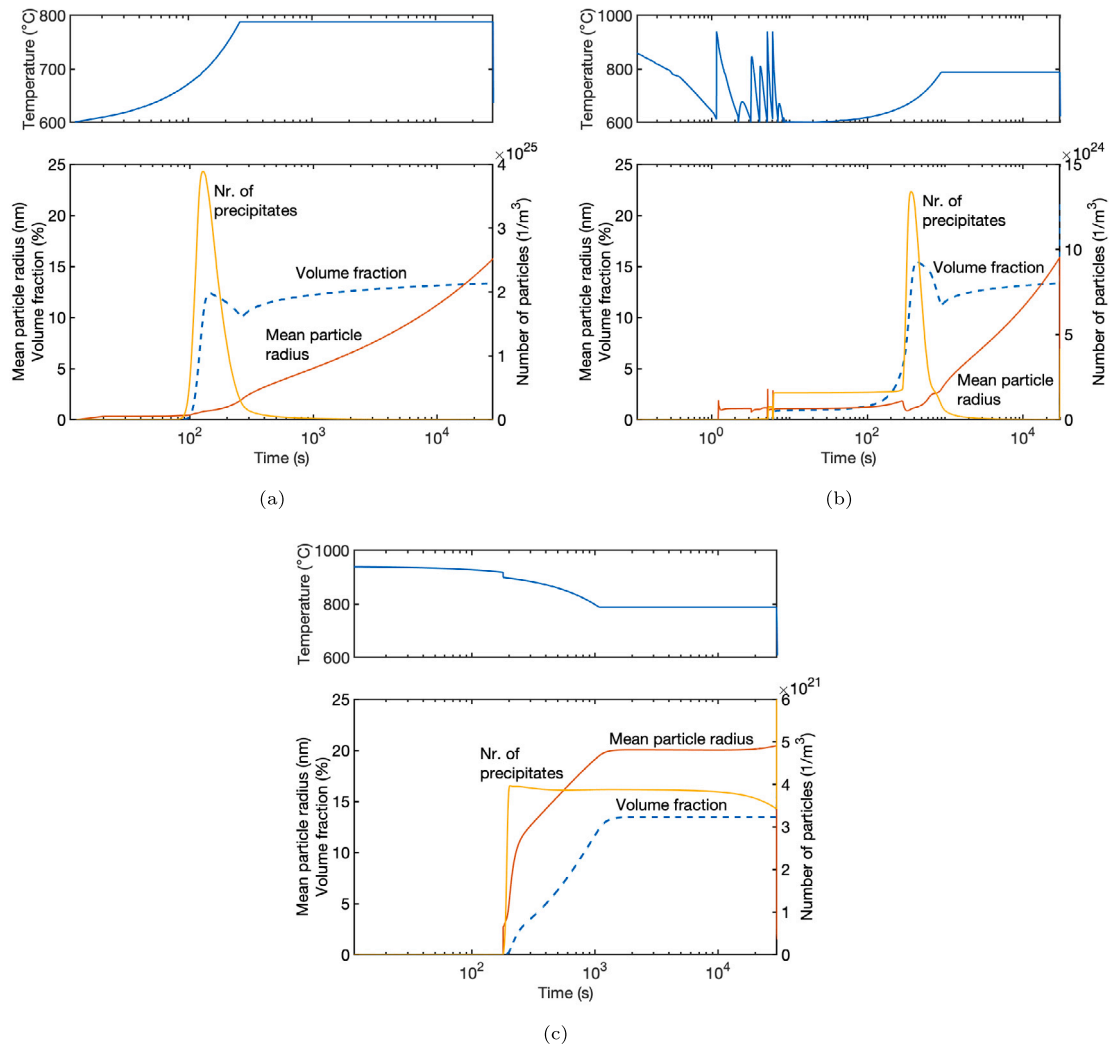


**Fig. 16.** Simulated precipitate evolution for the three scenarios: (a) scenario one, direct heat treatment; (b) scenario two, heat treatment with nuclei from the manufacturing process accounted for (sample no. 2); and (c) scenario three, heat treatment by slow cooling from 1010 °C (sample no. 3).

### CRedit authorship contribution statement

**Martin Fisk:** Writing – review & editing, Writing – original draft, Validation, Software, Project administration, Methodology, Funding acquisition, Formal analysis, Conceptualization. **Anders Ericsson:** Writing – review & editing, Writing – original draft, Software, Methodology, Formal analysis. **Manon Bonvalet Rolland:** Validation, Methodology, Formal analysis, Data curation, Conceptualization. **Erik Granhed:** Writing – review & editing, Methodology, Conceptualization. **Johan Hektor:** Writing – review & editing, Software, Methodology, Conceptualization. **Alexander Dahlström:** Writing – review & editing, Resources, Methodology. **Jesper Silwer:** Resources, Funding acquisition, Conceptualization. **Ceena Joseph:** Resources, Methodology, Funding acquisition, Conceptualization. **Petter Persson:** Writing – review & editing, Funding acquisition, Conceptualization. **Greta Lindwall:** Writing – review & editing, Validation, Project administration, Methodology, Funding acquisition, Conceptualization.

### Declaration of competing interest

The authors declare that they have no known competing financial interests or personal relationships that could have appeared to influence the work reported in this article.

### Acknowledgments

The authors acknowledge the Swedish Innovation Agency Vinnova for financial support of the *Generic Precipitation Model for FEM Coupled with the Calphad Approach (GEPRE)* project (grant no. 2019-02618) and the *LIGHTer Academy* project (grant no. 2023-01937), as well as the P21.2 Swedish Materials Science beamline at PETRA III, DESY, and especially Ulrich Leinert, Dr. Zoltan Hegedüs, and Dr. Malte Blankenburg, for technical support and guidance.

### Data availability

Data will be made available on request.

### References

- [1] I.J. Solomon, P. Sevel, J. Gunasekaran, P. Tanushkumar, A review on additive manufacturing of alloys using laser metal deposition, in: *Materials Today: Proceedings*, Vol. 64, Elsevier Ltd, 2022, pp. 44–50, <http://dx.doi.org/10.1016/j.matpr.2022.03.510>.
- [2] C. Selcuk, Joining processes for powder metallurgy parts, in: I. Chang, Y. Zhao (Eds.), *Advances in Powder Metallurgy*, in: Woodhead Publishing Series in Metals and Surface Engineering, Woodhead Publishing, 2013, pp. 380–398, <http://dx.doi.org/10.1533/9780857098900.3.380>.

- [3] L. Yan, Y. Chen, F. Liou, Additive manufacturing of functionally graded metallic materials using laser metal deposition, *Addit. Manuf.* 31 (2020) 100901, <http://dx.doi.org/10.1016/j.addma.2019.100901>, URL <https://linkinghub.elsevier.com/retrieve/pii/S2214860418308364>.
- [4] A. Ramakrishnan, G.P. Dinda, Functionally graded metal matrix composite of haynes 282 and sic fabricated by laser metal deposition, *Mater. Des.* 179 (2019) <http://dx.doi.org/10.1016/j.matdes.2019.107877>.
- [5] C. Joseph, *Microstructure Evolution and Mechanical Properties of Department of Industrial and Materials Science (Ph.D. thesis)*, Chalmers, 2018.
- [6] C. Joseph, C. Persson, M.H. Colliander, Influence of heat treatment on the microstructure and tensile properties of ni-base superalloy haynes 282, *Mater. Sci. Eng. A* 679 (2017) 520–530, <http://dx.doi.org/10.1016/j.msea.2016.10.048>.
- [7] S. Mukherjee, B.P. Sahu, S.K. Sarkar, S. Ahlawat, A. Biswas, G.K. Mandal, S. Tarafder, S.K. Kar, Temporal evolution of  $\gamma'$  precipitate in haynes 282 during ageing: growth and coarsening kinetics, solute partitioning and lattice misfit, *Materialia* 26 (2022) <http://dx.doi.org/10.1016/j.mtla.2022.101633>.
- [8] Q. Chen, et al., Tc-prisma user's guide and examples, 2011, (accessed 24 September 2025). URL <https://studylib.net/doc/18672725/tc-%E2%80%93prisma-user-s-guide-and-examples—thermo>.
- [9] S. Haas, J. Andersson, M. Fisk, J.S. Park, U. Lienert, Correlation of precipitate evolution with Vickers hardness in Haynes<sup>®</sup> 282<sup>®</sup> superalloy: In-situ high-energy SAXS/WAXS investigation, *Mater. Sci. Eng. A* 711 (2017) (2018) 250–258, <http://dx.doi.org/10.1016/j.msea.2017.11.035>.
- [10] C. Joseph, M. Thuvander, C. Persson, M.H. Colliander, Precipitation of  $\gamma'$  during cooling of nickel-base superalloy haynes 282, *Phil. Mag. Lett.* 101 (1) (2021) 30–39, <http://dx.doi.org/10.1080/09500839.2020.1841314>, arXiv:<https://doi.org/10.1080/09500839.2020.1841314>.
- [11] K. Thompson, D. Lawrence, D. Larson, J. Olson, T. Kelly, B. Gorman, In situ site-specific specimen preparation for atom probe tomography, *Ultramicroscopy* 107 (2) (2007) 131–139, <http://dx.doi.org/10.1016/j.ultramicro.2006.06.008>, URL <https://www.sciencedirect.com/science/article/pii/S0304399106001203>.
- [12] L. Tegg, A.J. Breen, S. Huang, T. Sato, S.P. Ringer, J.M. Cairney, Characterising the performance of an ultrawide field-of-view 3d atom probe, *Ultramicroscopy* 253 (2023) 113826, <http://dx.doi.org/10.1016/j.ultramicro.2023.113826>, URL <https://www.sciencedirect.com/science/article/pii/S0304399123001432>.
- [13] C. Hatzoglou, G. Da Costa, F. Vurpillot, Enhanced dynamic reconstruction for atom probe tomography, *Ultramicroscopy* 197 (2019) 72–82, <http://dx.doi.org/10.1016/j.ultramicro.2018.11.010>, URL <https://www.sciencedirect.com/science/article/pii/S0304399118300494>.
- [14] D.J. Larson, R.M. Ulfing, D.R. Lenz, J.H. Bunton, J.D. Shepard, T.R. Payne, K.P. Rice, Y. Chen, T.J. Prosa, D.J. Rauls, T.F. Kelly, N. Sridharan, S. Babu, Microstructural investigations in metals using atom probe tomography with a novel specimen-electrode geometry, *JOM* 70 (2018) 1776–1784, <http://dx.doi.org/10.1007/s11837-018-2982-1>.
- [15] M. Fisk, M. Ristinmaa, A. Hultkrantz, L.-E. Lindgren, Coupled electromagnetic-thermal solution strategy for induction heating of ferromagnetic materials, *Appl. Math. Model.* 111 (2022) 818–835, <http://dx.doi.org/10.1016/j.apm.2022.07.009>.
- [16] N. Saunders, Z. Guo, X. Li, A.P. Miodownik, J.-P. Schillé, Using jmatpro<sup>®</sup> to model materials properties and behaviour, *JOM* 55 (12) (2003) 60–65, <http://dx.doi.org/10.1007/s11837-003-0013-2>.
- [17] L.-E. Lindgren, *Computational Welding Mechanics: Thermomechanical and Microstructural Simulations*, CRC Press, 2007.
- [18] J. Goldak, A. Chakravarti, M. Bibby, A new finite element model for welding heat sources, *Metall. Trans. B* 15 (1984) 299–305, <http://dx.doi.org/10.1080/21681805.2017.1363816>.
- [19] L.-E. Lindgren, A. Lundbäck, M. Fisk, R. Pederson, J. Andersson, Simulation of additive manufacturing using coupled constitutive and microstructure models, *Addit. Manuf.* 12 (2016) 144–158, <http://dx.doi.org/10.1016/j.addma.2016.05.005>.
- [20] C. Balaji, B. Srinivasan, S. Gedupudi, Chapter 2 - one-dimensional, steady state heat conduction, in: C. Balaji, B. Srinivasan, S. Gedupudi (Eds.), *Heat Transfer Engineering*, Academic Press, 2021, pp. 15–64, <http://dx.doi.org/10.1016/B978-0-12-818503-2.00002-2>, URL <https://www.sciencedirect.com/science/article/pii/B9780128185032000022>.
- [21] A. Malmelöv, A. Lundbäck, L.E. Lindgren, History reduction by lumping for time-efficient simulation of additive manufacturing, *Metals* 10 (2020) <http://dx.doi.org/10.3390/met10010058>.
- [22] T. Philippe, P.W. Voorhees, Ostwald ripening in multicomponent alloys, *Acta Mater.* 61 (11) (2013) 4237–4244, <http://dx.doi.org/10.1016/j.actamat.2013.03.049>.
- [23] T. Philippe, D. Blavette, P.W. Voorhees, Critical nucleus composition in a multicomponent system, *J. Chem. Phys.* 141 (12) (2014) <http://dx.doi.org/10.1063/1.4896222>.
- [24] K.F. Kelton, A. Greer, *Nucleation in Condensed Matter: Applications in Materials and Biology*, first ed., Pergamon, Oxford, 2010, [http://dx.doi.org/10.1016/S1470-1804\(09\)01515-6](http://dx.doi.org/10.1016/S1470-1804(09)01515-6).
- [25] E. Kozeschnik, *Modeling Solid-State Precipitation*, Momentum Press, 2012, <http://dx.doi.org/10.5643/9781606500644>.
- [26] T. Philippe, M. Bonvalet, D. Blavette, Kinetic theory of diffusion-limited nucleation, *J. Chem. Phys.* 144 (20) (2016) <http://dx.doi.org/10.1063/1.4950878>.
- [27] M.G. Fahrman, D.A. Metzler, Simulation of  $\gamma'$  precipitation kinetics in a commercial ni-base superalloy, *JOM* 68 (2016) 2786–2792, <http://dx.doi.org/10.1007/s11837-016-2097-5>.
- [28] O.R. Myhr, O. Grong, Modelling of non-isothermal transformations in alloys containing a particle distribution, *Acta Mater.* 48 (7) (2000) 1605–1615, [http://dx.doi.org/10.1016/S1359-6454\(99\)00435-8](http://dx.doi.org/10.1016/S1359-6454(99)00435-8).
- [29] M. Perez, M. Dumont, D. Acevedo-Reyes, Implementation of classical nucleation and growth theories for precipitation, *Acta Mater.* 56 (9) (2008) 2119–2132, <http://dx.doi.org/10.1016/j.actamat.2007.12.050>.
- [30] Haynes International, Inc., Haynes<sup>®</sup> 282<sup>®</sup> alloy, 2023, <https://haynesintl.com/alloys/alloy-portfolio/high-temperature-alloys/haynes-282>, (accessed 17 September 2025).
- [31] J. Kieffer, J. Wright, Pyfai: a python library for high performance azimuthal integration on gpu, *Powder Diffr.* 28 (S2) (2013) S339–S350.
- [32] T. Perrin, G.A. Chahine, S. Arnaud, A. Després, P. Heugue, A. Deschamps, F.D. Geuser, Improving the reliability of small- and wide-angle x-ray scattering measurements of anisotropic precipitates in metallic alloys using sample rotation, *J. Appl. Crystallogr.* 57 (2024) 1800–1814, <http://dx.doi.org/10.1107/S1600576724009294>.
- [33] J.M. Schneider, B. Schönfeld, B. Demé, G. Kosterz, Shape of precipitates in ni-al-mo single crystals, in: *Journal of Applied Crystallography*, Vol. 33, 2000, pp. 465–468, <http://dx.doi.org/10.1107/S0021889800099969>.
- [34] C.E. Buckley, Interpretation of small angle x-ray scattering from aluminium single crystals, 2006, <http://dx.doi.org/10.1016/j.jallcom.2005.07.065>.
- [35] E.G. Dere, H. Sharma, R.M. Huiyenga, G. Portale, W. Bras, V. Bliznuk, J. Sietsma, S.E. Offerman, Formation of (fe, cr) carbides and dislocation structures in low-chromium steel studied in situ using synchrotron radiation, *J. Appl. Crystallogr.* 46 (2013) 181–192, <http://dx.doi.org/10.1107/S0021889812043531>.
- [36] Y. Ohmasa, A. Chiba, Intensity distribution profile of double bragg scattering in the small-angle region from highly oriented pyrolytic graphite, *Acta Crystallogr. Sect. A: Found. Adv.* 74 (2018) 681–698, <http://dx.doi.org/10.1107/S2053273318012469>.
- [37] J.S. Pedersen, Analysis of small-angle scattering data from colloids and polymer solutions: modeling and least-squares fitting, *Adv. Colloid Interface Sci.* 70 (1997) 171–210, [http://dx.doi.org/10.1016/S0001-8686\(97\)00312-6](http://dx.doi.org/10.1016/S0001-8686(97)00312-6), URL <http://linkinghub.elsevier.com/retrieve/pii/S0001868697003126>.
- [38] A. Ericsson, *Crystallization in Additive Manufacturing of Metallic Glass (Ph.D. thesis)*, Lund University, 2021.
- [39] M. Tidefelt, *Quantitative Characterization of Nanosized Precipitate Distributions in Glassy Alloys (Licentiate thesis in engineering)*, Malmö University, Malmö, 2024.
- [40] L. Kiss, J. Söderlund, G. Niklasson, C. Granqvist, The real origin of lognormal size distributions of nanoparticles in vapor growth processes, *Nanostruct. Mater.* 12 (1999) 327–332, [http://dx.doi.org/10.1016/S0965-9773\(99\)00128-2](http://dx.doi.org/10.1016/S0965-9773(99)00128-2), URL <https://linkinghub.elsevier.com/retrieve/pii/S0965977399001282>.
- [41] R.B. Bergmann, A. Bill, On the origin of logarithmic-normal distributions: An analytical derivation, and its application to nucleation and growth processes, *J. Cryst. Growth* 310 (2008) 3135–3138, <http://dx.doi.org/10.1016/j.jcrysgro.2008.03.034>.
- [42] X. Zhao, Y. Wang, X. Song, Y. Wang, Z. Chen, Segregation behavior of alloying elements and its effects on stacking fault of  $\gamma'$  phase in ni-based superalloys: First-principles study, *Comput. Mater. Sci.* 202 (2022) <http://dx.doi.org/10.1016/j.commatsci.2021.110990>.
- [43] M. Tidefelt, J. Löfstrand, I.K. Goetz, O. Donzel-Gargand, A. Ericsson, X. Han, P.E. Jönsson, M. Sahlberg, I. Kaban, M. Fisk, In situ mapping of phase evolutions in rapidly heated zr-based bulk metallic glass with oxygen impurities, *Adv. Sci.* 11 (2024) <http://dx.doi.org/10.1002/adv.202307856>.